# Rolling shutter-induced aberrations in laser guide star wavefront sensing

**Guido Agapito**,* **Lorenzo Busoni**,* **Giulia Carlà**, **Cédric Plantet**, **and Simone Esposito**
INAF—Osservatorio Astrofisico di Arcetri, Firenze, Italy

**Abstract.** Laser guide star (LGS) Shack–Hartmann (SH) wavefront sensors for next-generation Extremely Large Telescopes (ELTs) require low-noise, large format (∼1 Mpx), fast detectors to match the need for a large number of subapertures and a good sampling of the very elongated spots. One path envisaged to fulfill this need has been the adoption of complementary metal metal-oxide semiconductor detectors with a rolling shutter read-out scheme that allows low read-out noise and fast readout time at the cost of image distortion due to the detector rows exposed in different moments. Here, we analyze the impact of the rolling shutter read-out scheme when used for LGS SH wavefront sensing; in particular, we focus on the impact on the adaptive optics (AO) correction of the distortion-induced aberrations created by the rolling exposure in the case of fast varying aberrations, like the ones coming from the LGS tilt jitter due to the up-link propagation of laser beams. We show that the LGS jitter-induced aberration for an ELT can be as large as 100-nm root-mean-square, a significant term in the wavefront error budget of a typical AO system on an ELT, and we discuss possible mitigation strategies.  [DOI: 10.1117/1.JATIS.8.2.021505]

**Keywords:** adaptive optics; rolling shutter; laser guide stars; wavefront sensor; Extremely Large Telescopes.

Paper 21158SS received Dec. 7, 2021; accepted for publication Mar. 25, 2022; published online Apr. 25, 2022.

## 1 Introduction

Next-generation Extremely Large Telescopes (ELTs)[1–3] foresee the use of laser guide stars (LGSs) in their adaptive optics (AO) systems.[4–10] They all use Shack–Hartmann (SH) LGS wavefront sensors (WFSs) that are highly demanding in terms of detector's specifications.[11–14] In fact, a typical AO system assisting a near-infrared instrument requires a pupil sampling of the order of 0.5 m, resulting in $80 \times 80$ subapertures for a 39-m telescope. In addition, the need to avoid truncation of largely elongated LGS spots drives the design of LGS WFSs toward large field of views of the order of 10 to 15 arcsec[14] for LGSs launched from the telescope's side. On the other hand, the need to properly sample the spot along the non-elongated direction pushes the design to pixel scales of about 1 to 1.5 arcsec, in such a way that each subaperture requires $10 \times 10$ pixels or more. As a result, the SH LGS WFS for ELTs demands large format detectors, with more than $1000 \times 1000$ pixels in the ideal case. The readout noise is also an important parameter, because the LGS return flux is spread over tens of pixels in the most elongated spots resulting in an expected flux that can be as small as a few tens of photons per pixel. Finally, the speed is also a key requirement, with typical framerate ranging from 500 to 1000 fps for the considered systems.

Such a set of tight constraints for LGS WFS detectors has been identified as a critical aspect since the early stage of development of the ELTs.[15] It led, on one hand, to a variety of mitigation strategies spanning from control aspects[13,16] to new WFS optical design[17] and, on the other hand, to embrace the technological challenge of developing large format, fast, and low-noise detectors.[18–21]

*Address all correspondence to Guido Agapito, guido.agapito@inaf.it; Lorenzo Busoni, lorenzo.busoni@inaf.it

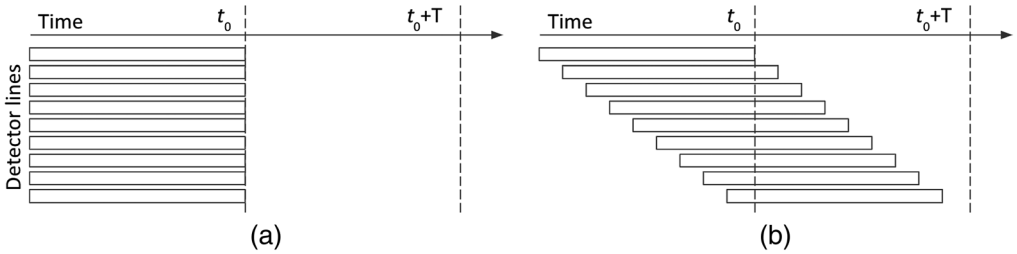


**Fig. 1** Diagram of the exposure timings: global shutter read-out (a) and rolling shutter top-bottom read-out (b). $t_0$ is the time when the readout begins and $T$ is the integration time. Each rectangle, $T$ seconds long, represents the exposure interval of each scanline. In rolling shutter detectors, the readout of each scanline begins right at the end of the exposure.

Wavefront sensing in AO systems is generally performed through charge-coupled device (CCD) sensors. CCDs operate under a global shutter regime, i.e., the sensor exposes all pixels simultaneously [see Fig. 1(a)] and transfers the signals to a few analog-to-digital converters. When dealing with a large amount of pixels, the read-out time can introduce a non-negligible latency into the AO control loop and limit the wavefront correction. In this context, an alternative solution foresees the use of complementary metal-oxide semiconductor (CMOS) sensors with a rolling shutter readout that allows for high efficiency and low noise preserving a high pixel rate to prevent a big penalization in latency. To date, rolling shutter sensors are planned to be used in astronomical AO on the ELT[22] and on the Subaru ground-layer AO system.[23]

In detectors using a rolling shutter read-out scheme, each scanline of the image is exposed at a different time and the readout of a line is happening while the other lines are still exposed to the light [see Fig. 1(b)]. This has an important effect on the average delay associated to the read-out, i.e., halved compared to the global shutter. The delay between the availability of a given scanline and the availability of the full-frame depends on the position of the line and goes linearly from the integration time to a value, i.e., the readout time of a single line. Rolling shutters are then able to reduce the temporal term of the error budget of an AO system, as shown in Ref. 24.

On the other side, when the sequential exposure is combined with a dynamically evolving object, it produces image distortions. In the case of an SH WFS, they result in displacements of the spot images within the subapertures, finally seen as biases in the WFS measures. The effect might not be negligible, especially in the case of LGS WFSs, where a large and fast PSF jitter due to the upward beam propagation is typically expected.

In the following, we analyze the impact of the rolling shutter read-out scheme on LGS SH wavefront sensing when dealing with fast-varying aberrations, and in particular, we focus on the LGS tilt jitter. We apply our analysis to the ELT case, hence all numerical examples consider a telescope diameter of 39 m and a typical LGS WFS framerate of 500 Hz, though we explicitly show the dependence on telescope radius and on WFS integration time in the analysis.

In Sec. 2, we quantify the residual LGS tilt in both amplitude and temporal evolution for a median atmospheric condition, taking into account a typical jitter compensation; in Sec. 3, we introduce a toy model for a rough estimation of the properties of the rolling shutter-induced aberration; in Sec. 4, we discuss the propagation of the aberrations in the main AO loop; in Sec. 5, we characterize the aberrations through numerical simulations; and in Sec. 6, we discuss open issues and possible mitigation strategies.

## 2 LGS Jitter

LGS tilt jitter is determined by turbulence-induced fluctuations introduced during both the upward and downward propagation of the laser beam. If we consider that the LGS tilt is given by the difference between the upward tilt and the downward one, where the difference is representative of the two waves propagating in the opposite directions,[25] we can write the temporal power spectral density (PSD) of LGS tilt jitter as

$$P_{\mathrm{LGS}}(\nu) = P_{\mathrm{up}}(\nu) + P_{\mathrm{down}}(\nu) - 2P_{\mathrm{up,down}}(\nu), \tag{1}$$

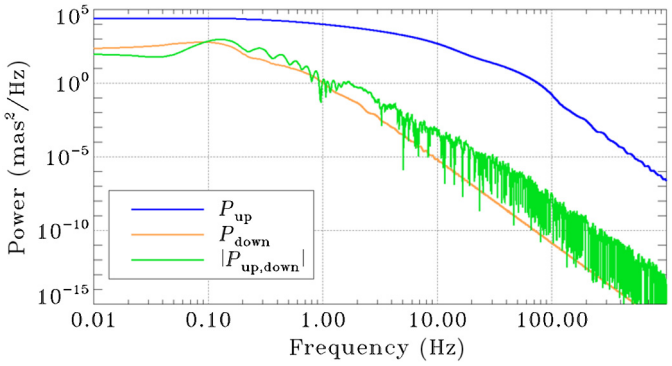


**Fig. 2** Tilt PSDs for the upward (blue) and downward (orange) propagation, and cross PSD between the upward and downward beam (green).

where $\nu$ is the temporal frequency; $P_{up}$ and $P_{down}$ are PSDs of the tilt seen, respectively, on the upward and downward beam; and $P_{up,down}$ is the cross PSD of the tilt between the two beams.[26]

In the ELT case, the upward and downward beam have a diameter of 0.4 and 39 m, respectively. As the angular jitter variance depends on the diameter as $D^{-1/3}$, the upward term gives the dominant contribution to the LGS tilt jitter energy and it also represents the fastest signal, as the cut-off frequency depends on the inverse of the aperture diameter ($\nu_{cutoff} \sim V/D$, with $V$ the wind velocity).[27] This is shown in Fig. 2, where the curves are obtained for the ELT median turbulence profile reported in Ref. 28, with a zenith angle of 30 deg, a seeing of 0.7 arcsec and an average wind speed of 9.2 m/s. We estimate the amount of LGS tilt jitter from these PSDs, and we get a standard deviation of 200 mas.

We consider then that the signal is compensated by a closed loop (see Fig. 3) where the control, $C_\theta$, is a pure integrator and the plant, $G_\theta$ is approximated as a pure delay of 3 frames (1 due to read-out, 1 due to sample and hold, 0.5 due to real-time computer and 0.5 due to deformable mirror response time), with a frame period of 2 ms. In this computation, we are considering that the actuator correcting the LGS jitter is hosted in the LGS WFS itself, so we neglect the propagation time of the LGS beam. If, on the contrary, the jitter compensator is hosted in the laser launch telescope, one has to consider also the delay due to the round-trip propagation of the laser beam to the sodium layer, resulting in 0.7 ms (0.35 frames). Assuming that the power of the measurement noise $v$ is 0.01 of the turbulence power, we find that the residual is minimized by a gain of about 0.35 and we get a residual jitter standard deviation of 58 mas (in good agreement with Refs. 29 and 30). The PSD of the input and residual disturbances are shown in Fig. 4.

In the following sections, we will use these results, though it is worth noting that the amount of residual jitter varies according to the atmospheric conditions. We find that the value ranges from 44 to 89 mas when considering 0.5 and 1.1 arcsec of seeing (i.e., first and last seeing quartile of the ELT turbulence profile at 30 deg of zenith angle). The mean wind speed is also a relevant parameter, as it moves the cut-off frequency of the input PSD with respect to the rejection bandwidth of the loop, thus making the correction more or less effective. If we consider 0.5 or 2 times the mean wind speed (4.6 and 18.4 m/s, respectively) of the median profile,

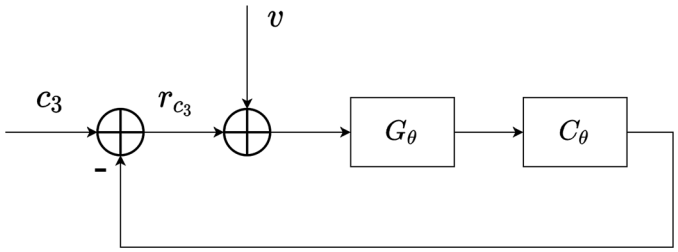


**Fig. 3** Diagram of the laser jitter closed loop. $G_\theta$ is the plant, $C_\theta$ is the control, $c_3$ is the incoming tilt, $r_{c_3}$ is the residual of the tilt, and $v$ is the measurement noise.

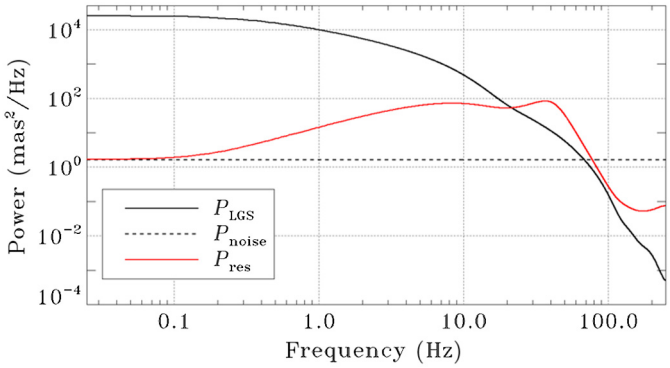


**Fig. 4** Tilt PSDs of the input disturbances and of the residual jitter.

we get a residual jitter standard deviation of 31 and 97 mas, respectively. Finally, if we increase the airmass with a zenith angle of 60 deg, we get 69 mas.

## 3 Toy Model for Rolling Shutter-Induced Aberrations in LGS SH WFS

In this section, we present an oversimplified model to estimate the order of magnitude of the aberration caused by the rolling shutter read out in an LGS-driven AO system for an ELT.

Let us assume as a fact that the LGS residual jitter has an amplitude of ~60 mas root-mean-square (RMS) with a PSD peaked at ~10 Hz, as shown in Sec. 2. Let us oversimplify the analysis by assuming a one-dimensional model where the LGS spot in the telescope focal plane follows an harmonic trajectory $\theta(t)$

$$\theta(t) = A\ \sin(2\pi t/T_j), \tag{2}$$

with period $T_j = 100$ ms and amplitude ~60 mas RMS, corresponding to $A = 100$ mas. The maximum jitter speed is $\dot{\theta}_{\max} = \frac{2\pi A}{T_j} \sim 6$ mas/ms and let us assume in the toy model that during an exposure period $T$ of 2 ms (corresponding to a typical LGS WFS framerate of 500 Hz) the jitter speed is constant, of modulus $\dot{\theta}_{\max}$, and parallel to the LGS WFS detector columns (direction $y$) so that the LGS spot moves by $\Delta\theta = \dot{\theta}_{\max} T = 12$ mas during a single frame exposure. Let us consider that the LGS SH WFS detector is using a rolling shutter read-out scheme where the subapertures are read sequentially from top to bottom [see Fig. 1(b)]. Let us also assume for simplicity that each row of subapertures is read in exactly one readout period, in such a way that the spot within each subaperture is imaged in a "global shutter" way. This feature is available in some rolling shutter detectors having $m$ rows read in groups of $k$ rows for a total of $n = m/k$ readout periods; in the assumption done above, we assume subapertures of $k \times k$ pixels.

During the exposure periods, the LGS spot will move with the aforementioned law of motion, creating a wavefront slope signal that increases linearly along the $y$ direction (see Fig. 5). The slope difference between the first and the last row of subapertures is $\Delta s_y = \Delta\theta = 12$ mas and let us assume that the slope average is null over the pupil so that the $y$ slopes measured in the first and last subaperture rows are $s_y^{\text{edge}} = \Delta s_y/2 = 6$ mas and $-s_y^{\text{edge}}$, respectively, and scale linearly in between. The wavefront gradients measured by an SH WFS are therefore

$$\frac{\partial\phi(x,y)}{\partial y} \propto y, \quad \frac{\partial\phi(x,y)}{\partial x} = 0, \quad \left.\frac{\partial\phi(x,y)}{\partial y}\right|_{y=R} = s_y^{\text{edge}}, \quad \left.\frac{\partial\phi(x,y)}{\partial y}\right|_{y=-R} = -s_y^{\text{edge}}, \tag{3}$$

and correspond to a cylindric-shaped wavefront, which can be expressed as

$$\phi(x,y) = 4c_{\text{cyl}}\left(\frac{y^2}{R^2} - 1\right) = \frac{c_{\text{cyl}}}{\sqrt{3}}\left[Z_4\left(\frac{x}{R},\frac{y}{R}\right) + \sqrt{2}Z_6\left(\frac{x}{R},\frac{y}{R}\right)\right], \tag{4}$$

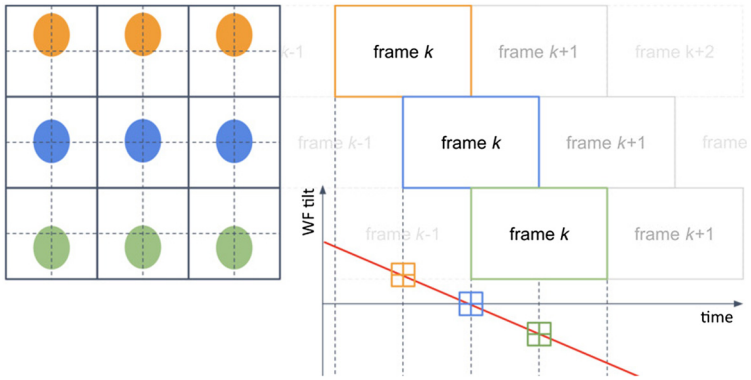


**Fig. 5** A schematic representation of the rolling shutter-induced distortion in a SH WFS in the case of a fast evolving tilt (spot moving along the columns of the detector). In this example, the WFS is a $3 \times 3$ SH and the entire detector is read in 3 blocks of rows; each block is exposed during different intervals highlighted in orange, blue and green. The time-average of the WF tilt during the exposure intervals is visualized by the three cross symbols and corresponds to the SH spot offset in the 3 blocks of subapertures: in the example, the top row of subapertures sensed the wavefront when the tilt was slightly positive, the central row sensed a null tilt, the bottom row sensed a negative tilt resulting in the overall frame shown on the left. The resulting SH spot pattern is distorted, indistinguishable from the one of a cylindrical wavefront aberration, as described in the text.

where the normalization is chosen to have $\sigma_\phi = c_{\text{cyl}}$ over the pupil of radius $R$ and $c_{\text{cyl}}$ must be determined to fulfill Eq. (3). $Z_4$ and $Z_6$ are Noll's Zernike polynomials for the focus and the astigmatism at 0 deg.[31] From derivation of Eq. (4), the slope at the pupil edge is

$$\left.\frac{\partial \phi(x,y)}{\partial y}\right|_{y=R} = \frac{8\, c_{\text{cyl}}}{R}. \tag{5}$$

Therefore, the amplitude of the cylinder mode having slope at the pupil edge equal to $s_y^{\text{edge}}$ is

$$c_{\text{cyl}} = \frac{s_y^{\text{edge}} R}{8}. \tag{6}$$

For an $R = 19.5$ m telescope and $s_y^{\text{edge}} = 6$ mas $= 29$ nrad, we obtain $c_{\text{cyl}} = 71$ nm.

So, in the crude model considered above, the residual LGS jitter will create random spurious signals on the SH LGS WFS, corresponding to a cylindrical aberration of amplitude up to 71 nm RMS and 284-nm PtV, which is a considerable aberration for a typical AO system on the ELT. In fact, the error budget of ESO's ELT laser-based systems, such as HARMONI and MAORY (see Plantet et al. and Neichel et al. this review), is of the order of 300 nm. Obviously, the AO system will try to correct for these signals, injecting the corresponding aberration in the control loop, as described in Sec. 4.

In reality, the jitter speed is not constant throughout a frame exposure, neither in amplitude nor in direction and, as it can be seen in Appendix, a non-zero $\partial^k \theta / \partial t^k$ corresponds to a distortion-induced aberration (DIA) of radial degree $k+1$; so, more generically, the wavefront corresponding to the rolling shutter-induced signals will be a combination of focus and higher-order modes that will evolve with the same speed as the jitter derivatives. A more generic and accurate formalism to relate wavefront residual to DIA is presented in Appendix.

A note on the scaling with the telescope radius $R$: a given jitter $\theta$ expressed as on-sky angle in arcseconds corresponds to a Zernike tilt $Z_3$ whose amplitude in meter RMS is $c_3 = \theta R/2 \times 4.84810^{-6}$; for a $R = 39$ m telescope the conversion factor is 47 nm RMS/mas, which means that the wavefront amplitude for a 60-mas jitter is as large as 2.8 $\mu$m RMS.

For a given tilt amplitude speed $\dot{c}_3$, the tilt variation during an exposure is $\Delta c_3 = \dot{c}_3 T$, corresponding to an angular jitter $\Delta\theta = 2\dot{c}_3 T/R$, hence $s_y^{\text{edge}} = \dot{c}_3 T/R$. Combining with Eq. (6), we obtain the relation between the speed of the tilt coefficient and the amplitude of the distortion-induced cylinder

$$c_{\text{cyl}} = \frac{\dot{c}_3 T}{8}. \tag{7}$$

As a final comment for this section, we note that a tip jitter in the direction $x$, i.e., along the detector rows, is also creating rolling shutter-induced aberrations. In fact, in a similar way to what discussed above, there will be a bias in the $x$ signals scaling linearly from $s_x^{\text{edge}}$ in the top row of subapertures to $-s_x^{\text{edge}}$ in the bottom row, whereas $s_y$ will be null everywhere. The described gradient field clearly has non-zero curl, so, from a strict geometrical standpoint, there is no wavefront whose gradient corresponds to the measured signals. The typical wavefront reconstruction process will anyhow reconstruct a surface whose gradients best-fit the measured signals and that, in the tip case, corresponds to an xy-astigmatism. This will be shown in Sec. 5.

## 4 Propagation in the Closed Loop

In this section, we present how the residual tip and tilt described in Sec. 2 propagates to DIA and, finally, to the AO residual. We do not know the dynamics of the residual tip and tilt during a single exposure, but we can approximate, for simplicity, that tip and tilt is evolving in time with constant speed (because the time scales of the residual jitter are much larger than typical exposure times of 1 to 2 ms). It is worth noting that more realistic dynamics will induce higher-order aberrations, as it is shown in Appendix. Hence, considering a constant speed temporal evolution, the PSD of the tilt speed, $P_{\dot{c}_3}(\nu)$ is

$$P_{\dot{c}_3}(\nu) = \|H(z)\|^2 P_{c_3}(\nu), \tag{8}$$

where $\nu$ is the temporal frequency, $z = e^{j2\pi\nu T}$, $P_{c_3}(\nu)$ is the PSD of the tilt, and $H(z)$ is the transfer function (TF) between position and average speed on an interval $T$

$$H(z) = \frac{1}{T}(1 - z^{-1}). \tag{9}$$

From the PSD of the tilt speed and using Eq. (7), we can easily compute the PSD of the amplitude of the cylinder mode, $P_{\text{cyl}}(\nu)$

$$P_{\text{cyl}}(\nu) = \left(\frac{T}{8}\right)^2 P_{\dot{c}_3}(\nu) = \frac{T^2}{64}\|H(z)\|^2 P_{c_3}(\nu). \tag{10}$$

This PSD is filtered by the complementary sensitivity function, $W(z)$, and the residual variance of the cylinder, $\sigma^2_{\text{cyl}}$, is

$$\sigma^2_{\text{cyl}} = \frac{T^2}{64}\sum_{\nu=\Delta\nu}^{1/(2T)} \|W(z)H(z)\|^2 P_{c_3}(\nu)\Delta\nu, \tag{11}$$

where $\Delta\nu = 1/(2nT)$ and $n$ is the length of the PSD vector. The diagram of the propagation of the cylinder DIA in closed loop is shown in Fig. 6. Given a closed loop where the plant is modeled as a pure delay of $d$ frames, $G(z) = z^{-d}$, and the control is a pure integrator with gain $g$, $C(z) = g/(1 - z^{-1})$, the complementary sensitivity function is

$$W(z) = \frac{C(z)G(z)}{1 + C(z)G(z)} = \frac{gz^{-d}}{1 - z^{-1} + gz^{-d}}, \tag{12}$$

and the residual variance

$$\sigma^2_{\text{cyl}} = \frac{1}{64}\sum_{\nu=\Delta\nu}^{1/(2T)} \left\| \frac{g(z^{-d} - z^{-d-1})}{1 - z^{-1} + gz^{-d}} \right\|^2 P_{c_3}(\nu)\Delta\nu. \tag{13}$$

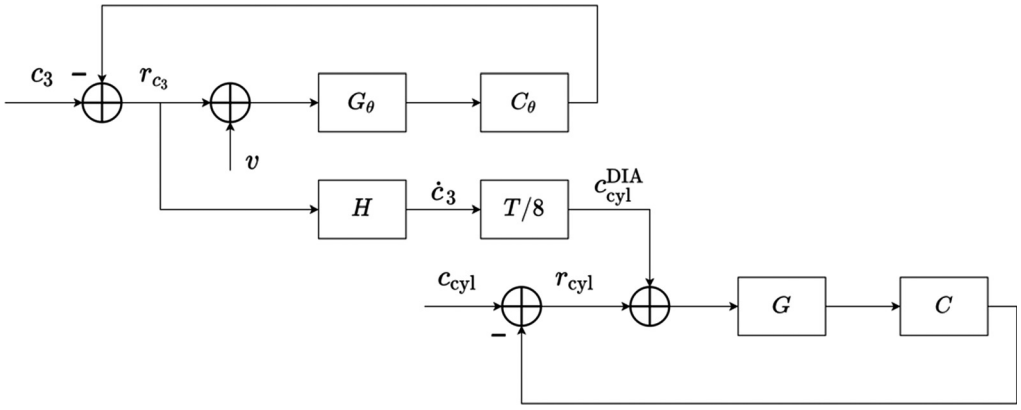


**Fig. 6** Diagram of the propagation of the cylinder in the closed loop. $G_\theta$ is the jitter plant, $C_\theta$ is the jitter control (presented in Sec. 2), $H$ is the position to speed conversion function, $T/8$ is the tilt speed to cylinder DIA conversion coefficient, $G$ is the plant, $C$ is the control, $c_3$ is the incoming tilt, $r_{c_3}$ is the tilt residual, $\dot{c}_3$ is the tilt speed, $v$ is the measurement noise, $c_{\text{cyl}}$ is the incoming cylinder, $r_{\text{cyl}}$ is the cylinder residual, and $c_{\text{cyl}}^{\text{DIA}}$ is the cylinder DIA.

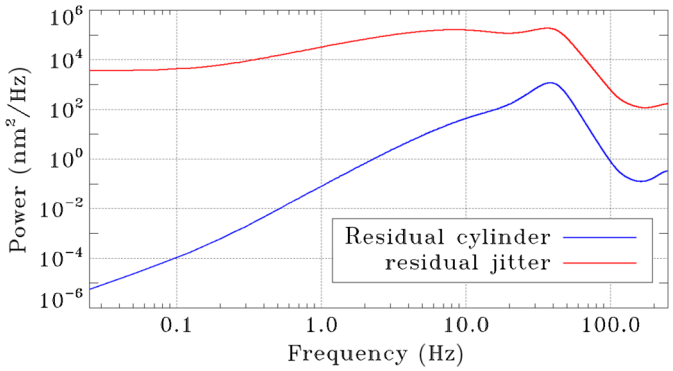


**Fig. 7** PSDs of the input residual LGS jitter and of the rolling shutter-induced cylinder after propagation into the AO loop.

Considering $T = 2$ ms, $d = 3$, and $g = 0.3$ and the residual jitter PSD shown in Sec. 2, we get a residual cylinder amplitude of 158-nm RMS (which means a SR reduction factor of about 0.5, 0.7, and 0.8 on the $J$, $H$, and $K$ band, respectively). Its PSD is shown in Fig. 7. It is worth noting that the residual RMS is proportional to the telescope diameter, so this value is scaled by 0.205 for an 8-m telescope.

## 5 Numerical Analysis

We set up a basic simulation with PASSATA[32] to numerically study the rolling shutter effect. We model the detector as a series of "temporal averaging functions" working in parallel and sensing a rectangular subregion of the full pupil corresponding to a single row of subapertures; we mimic the rolling shutter by setting a specific delay for the starting of the integration with respect to the simulation clock time in each of the temporal averaging functions. The number of temporal averaging functions, the size of the rectangular subregion, and the integration time and delay are programmable. In the following, we consider a $60 \times 60$ subapertures SH sensor and two read-out sequences:

1. Read-out sequence #1 [top to bottom, Fig. 1(a)]: each line of subapertures is read out in sequence, so there are 60 readouts, with delay going linearly from 0 to $59/60T$.
2. Read-out sequence #2 (edge to center): in parallel on the two halves of the detector (from the top row to the central row in the upper part of the detector and from the bottom row to

the central row in the lower part), each line of subapertures is readout in sequence, so there are 30 readouts for each half of the detector, with delay going linearly from 0 to $29/30T$.

We set the simulation temporal step to 1/60 of $T$ to allow the correct simulation of the temporal averaging function. Finally, we use a circular pupil without central obstruction, and we expand the computed wavefronts and wavefront gradients on a Zernike modal base with 1000 modes.

As a first analysis, we impose a ramp of tip and tilt with constant speed of 1 nm/$T$ and we decompose the result of the reconstructed wavefront on the Zernike modal base. The results, summarized in Fig. 8, show that the tilt induces aberration of 0.07 nm on $Z_4$ and 0.1 nm on $Z_5$, corresponding to 0.125 nm of the cylinder mode defined in Eq. (4), for the first read-out mode, in agreement with the results of Sec. 3 and Eq. (7). In the case of the second read-out mode, DIAs are mostly (98% of the total RMS) distributed over comas and trefoils instead of focus and astigmatisms as in the first read-out mode.

We replicate the analysis applying a ramp of 1 nm/$T$ on the first 100 modes, and we report the quadratic sum of all aberration-induced distortions in Fig. 9.

The propagation of DIA shown in Fig. 9 is larger for higher-order modes than for tip and tilt, but the high-order residuals for a typical AO system will presumably have much smaller amplitude and slower evolution compared to the LGS spot residual jitter. A detailed quantification of the rolling shutter-induced aberrations taking into account the entire wavefront residual is specific to the AO system itself and is left for a future work. In the following, we focus again on the LGS jitter as the sole source of induced aberrations.

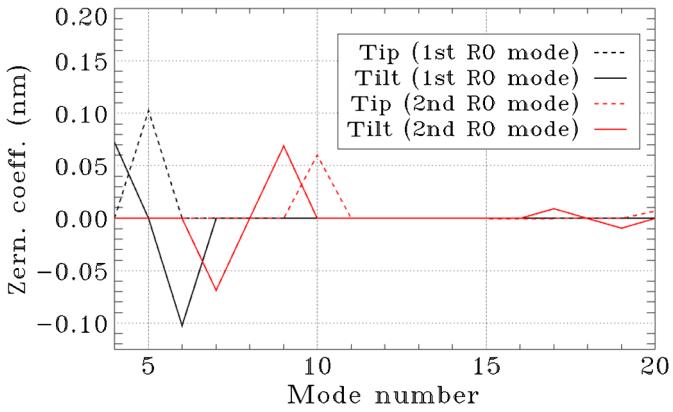


**Fig. 8** Value of the Zernike polynomials coefficient of the aberrations induced on first 20 Zernike modes (starting from number 4, which is focus) for tip and tilt ramp of 1-nm RMS in one integration time.

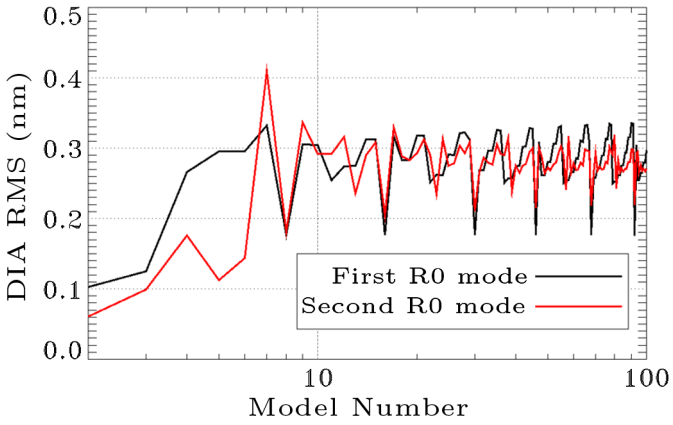


**Fig. 9** Quadratic sum of the aberration induced on higher modes by a ramp of 1 nm/$T$ applied to a given Zernike mode (from tip, number 2, to mode number 100).

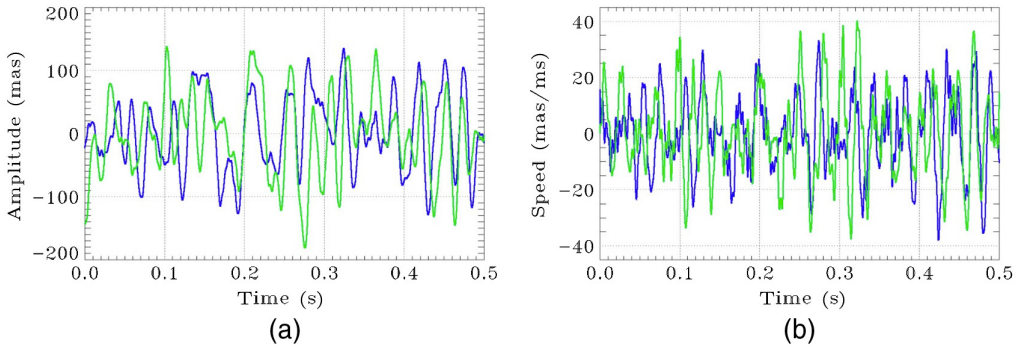


**Fig. 10** First 0.5 s of the first temporal random sequence of tip (blue) and tilt (green) drawn from PSD shown in Fig. 4 for both (a) amplitude and (b) speed.

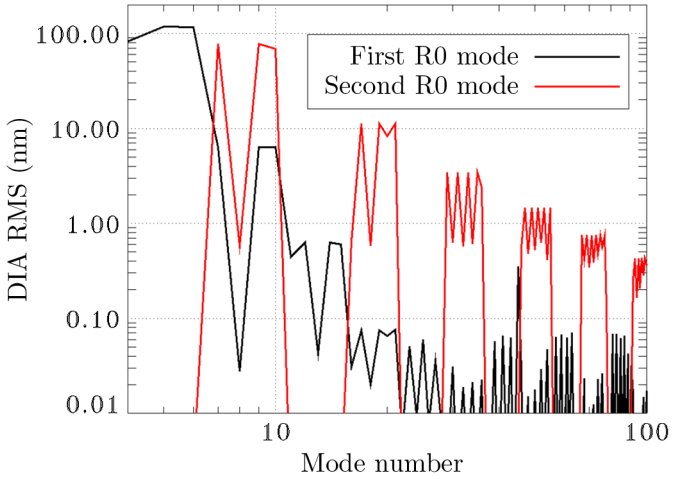


**Fig. 11** Aberrations induced by tilt distortion with 55-mas jitter per axis and PSD shown in Fig. 4.

To consider a more realistic input, we compute five random temporal sequences of 2 s of residual LGS jitter (on both tip and tilt) using the PSD shown in Sec. 2. The first random sequence is shown in Fig. 10. We compute the temporal variance of the induced aberration, shown in Fig. 11, after decomposition on the Zernike basis. In the case of the read-out sequence #1, the residual jitter is converted into a DIA of 185-nm RMS; the worst offender modes are the ones of the second radial order having amplitude of about 100-nm RMS. For the read-out sequence #2, the DIA is 132-nm RMS, with modes of the third radial order having amplitude of about 50-nm RMS. It is worth noting that after the propagation in the AO loop presented in Sec. 4, these values scales of about 1.2, becoming 217- and 162-nm RMS, respectively, for the read-out sequence #1 and #2 (corresponding to a K band SR scaling factor of about 0.7 and 0.8). As also reported in the previous sections, these errors will have an important impact on ESO's ELT laser-based systems, such as HARMONI and MAORY, whose maximum SR in K band is of the order of 50% (see Refs. 33 and 34).

Note that there are higher-order aberrations than the one expected for a constant speed temporal evolution (see Fig. 8 for reference, where read-out sequence #1 does not induce any aberrations on modes higher than astigmatisms), because, obviously, the tip and tilt jitter evolves with more complex dynamics than a simple constant speed law.

## 6 Discussion

The analysis presented so far has been focused on the main aspects of LGS wavefront sensing in ELTs in the case a rolling shutter detector is employed. There are some items that have not been considered in this work but deserve to be highlighted to trace possible future works.

First, as already stated in the previous sections, we deliberately exclude the effect of the rolling shutter in the formation of the image within each SH WFS subaperture: for the sake of simplicity, we consider that each subaperture is exposed in a global shutter way. In fact, the rows of each subaperture will be read in several readouts, creating a distorted spot in each subaperture. The impact on the centroiding algorithm of the spot distortion is still to be evaluated, and it could lead to an additional error term in the wavefront correction.

A second important point to consider is that LGSs will be used in ELTs for multi-WFS AO systems (ground layer AO, laser tomography AO, or multi-conjugate AO). In such systems, we want the same part of the pupil to be exposed synchronously on every WFS to avoid differential measurements induced by the temporal evolution that will be reconstructed as high order modes on a plane non-conjugated to the pupil. This requires the same readout sequence but it also requires the same clocking geometry between the pupil and the detector for all the WFSs. Unfortunately, to minimize truncation effects, one usually wants to clock the WFSs in such a way that the most elongated spots lay along the diagonal of the subapertures[35] in a way that, depending on the laser launch geometry, can be incompatible with the previous requirement.

While the typical use for a rolling shutter detector is within LGS WFSs for the reasons shown in the introduction, it is worthwhile to also consider the impact on NGS-based systems. In fact, in some cases the residual dynamics of such systems could produce not negligible DIA: for examples, wind shake and vibrations could impact some modes with amplitude or bandwidth so large to cause significant propagation into DIAs. Another condition that deserves deeper analysis is the transient state after enabling the AO correction: in this interval the wavefront aberrations can be large enough to cause significant propagation of DIAs, potentially impacting on the loop boot stability. Systems based on a Pyramid WFS,[36] where the WFS signals are obtained from sets of 4 pixels on 4 sub-pupils spatially separated on the detector, are also not immune from the rolling shutter effect, although in a more complex way that in the SH WFS case. In the case of a modulated pyramid WFS, the synchronization between modulation and exposure interval will also play a role in defining the DIAs.

Finally, we briefly outline a couple of possible strategies to reduce the rolling shutter-induced aberrations. A first option would be to modify the wavefront control architecture and use NGSs, instead of LGSs, to control the modes particularly affected by the induced aberrations. This requires an increase in the spatial sampling of the NGS WFS, typically designed to sense tip and tilt only[37] to also sense second order modes (for read-out sequence #1) or even third order modes (for read-out sequence #2). Clearly this approach has a major drawback on noise propagation and significantly affects the system's sky coverage. On this line, note that the LGS jitter evolution is fast enough that the rolling shutter-induced aberration cannot be disentangled from the atmospheric aberrations and corrected by a slow reference loop based on NGS measurements as is typically done to compensate pseudo-static biases due to instrument flexures or sodium profile variations.[38–43]

In a second mitigation option, following a scheme commonly used to compensate for rolling shutter-induced distortions,[44,45] one could forecast the tilt temporal evolution using the LGS WFS measurements from the previous steps. The estimated jitter dynamic can be used to compute the biased signals expected in the next exposure (see Appendix) and subtract the DIA from the reconstructed wavefront. The forecast of turbulence has been already studied and demonstrated in AO,[46–50] with good results in terms of PSF jitter stabilization; for the specific LGS case considered in this work, one has to note that the tilt signal given by the upward beam propagation is more challenging to forecast compared to the typical downward propagation because of its large power at higher temporal frequencies (see Fig. 4). Moreover, one has to also consider other source of errors, such as measurement noise, spatial aliasing, and WFS non-linearity due to spot elongation/truncation[51] that will limit the accuracy in forecasting the LGS jitter, hence limiting the correction effectiveness.

Finally, we note that we only explored two possible read-out sequences, with read-out sequence #2 being the most common one in current devices. A clever sequencing of the line scanning, tailored on the number of subapertures and on the number of pixel per subapertures could help in reducing the difference of the sampling time between the rows of subaperture, hence reducing the induced aberrations. This approach would obviously encounter limitations in terms of possible hardware implementation.

## 7 Conclusion

We have analyzed the effect of the image distortion in a gradient WFS equipped with a detector using a rolling shutter read-out scheme. Specifically, we have focused our analysis on LGS WFSs for ELTs, i.e., the AO application where rolling shutter CMOS detectors are particularly attractive because of their large format, low-noise, and low-latency features. We have investigated how a time-evolving aberration couples with the sequential scanning exposure and gives rise to an aliasing effect into modes of higher radial degree. A typical residual LGS jitter of 60 mas, although negligible in terms of tilt signal for an ELT LGS WFS, corresponds to a large residual aberration of ~3-$\mu$m RMS and propagates rolling shutter-induced aberration of more than 100-nm RMS on modes of the second radial order and above. The DIA evolves with the same bandwidth of the aberration that created it, making it difficult to decouple it from the atmospheric residual. Techniques to mitigate the effect of the rolling shutter-induced aberrations do exist and the most promising ones are based on the forecast of the residual aberrations.

## 8 Appendix: Formalism to Estimate Signals in a Rolling-Shutter-Based Gradient WFS

In this section, we present a generic formalism to compute the signals of a gradient wavefront sensor based on a rolling shutter detector, and we apply it to a few notable cases for verification purpose.

We consider a full circular pupil, and we adopt a reference system with origin in the center of the pupil, the $y$ axis parallel to the detector columns, and unitary pupil radius.

We describe the wavefront to be measured as developed on a series of Zernike polynomials[31] $Z_i$ whose amplitude $c_i$ depends on the time:

$$\phi(x, y, t) = \sum_{i=1}^{\infty} c_i(t) Z_i(x, y). \tag{14}$$

We suppose a rolling shutter exposure sequence where all the subapertures at coordinates $y$ are exposed in the temporal interval from $D(y)$ and $D(y) + T$, where $D(y)$ denotes the delay of start of integration of the line in $y$. Again, we consider that each subaperture is exposed in a global shutter way, i.e., we do not consider individual pixels readout but we simplify the model as if all the detector lines belonging to a given subaperture were exposed in the same interval.

The WFS $y$ gradient signals are as follows:

$$\begin{aligned} S_y(x, y) &= \frac{1}{T} \int_{D(y)}^{D(y)+T} \frac{\partial \phi}{\partial y}(x, y, t) \mathrm{d}t, \\ &= \frac{1}{T} \sum_{i=1}^{\infty} \frac{\partial Z_i}{\partial y}(x, y) \int_{D(y)}^{D(y)+T} c_i(t) \mathrm{d}t. \end{aligned} \tag{15}$$

In the case of read-out sequence #1 (top to bottom), the delay $D$ becomes:

$$D(y) = T \frac{y}{2}, \tag{16}$$

while in the case of read-out sequence #2 (edge to center) the delay $D$ reads:

$$D(y) = T(1 - |y|). \tag{17}$$

We can describe the temporal evolution of the amplitude of mode $i$ with a polynomial series:

$$c_i(t) = \sum_{k=0}^{\infty} a_k^i t^k. \tag{18}$$

Substituting Eq. (18) in Eq. (15), we obtain:

$$
\begin{aligned}
S_y(x,y) &= \frac{1}{T}\sum_{i=1}^{\infty}\frac{\partial Z_i}{\partial y}(x,y)\int_{D(y)}^{T+D(y)}\sum_{k=0}^{\infty}a_k^i t^k \mathrm{d}t,\\
&= \sum_{i=1}^{\infty}\frac{\partial Z_i}{\partial y}(x,y)\frac{1}{T}\sum_{k=0}^{\infty}a_k^i\frac{t^{k+1}}{k+1}\Bigg|_{t=D(y)}^{t=D(y)+T},\\
&= \sum_{i=1}^{\infty}\frac{\partial Z_i}{\partial y}(x,y)\sum_{k=0}^{\infty}\frac{a_k^i}{T(k+1)}[(T+D(y))^{k+1}-D(y)^{k+1}].
\end{aligned}
\tag{19}
$$

It is worth noting that this relation can be easily extended to the signal $S_x$ along the $x$ direction simply substituting $\partial Z_i/\partial y$ with $\partial Z_i/\partial x$. In Eq. (19), we recognize that the signal measured for every mode $i$ is the actual gradient of the $i$'th mode multiplied by a polynomial in $y$, described by the series in $k$. Hence, the reconstruction process will reconstruct modes of order equal and higher than $i$, whose amplitude depends on $a_k^i$, in a kind of inverse aliasing where every aberration of a given spatial frequency can contribute to DIAs of higher spatial frequencies.

### 8.1 *Global Shutter Case*

In the case of a global shutter detector, $D(y)=0$ and Eq. (19) simplifies to

$$
S_y(x,y) = \sum_{i=1}^{\infty}\frac{\partial Z_i}{\partial y}(x,y)\sum_{k=0}^{\infty}\frac{a_k^i T^k}{(k+1)} = \sum_{i=1}^{\infty}\frac{\partial Z_i}{\partial y}(x,y)\bar{c}_i,
\tag{20}
$$

where $\overline{c_i}$ denotes the time-average over the period $T$ of the modal amplitude $c_i$. The result in Eq. (20) shows the expected behaviour of a global shutter gradient wavefront sensor.

### 8.2 *Rolling Shutter Case: Top-Bottom Read-Out Sequence*

We can substitute Eq. (16) for the read-out sequence #1 in Eq. (19) and we get

$$
\begin{aligned}
S_y(x,y) &= \sum_{i=1}^{\infty}\frac{\partial Z_i}{\partial y}(x,y)\sum_{k=0}^{\infty}\frac{a_k^i T^k}{k+1}\left[\left(1+\frac{y}{2}\right)^{k+1}-\left(\frac{y}{2}\right)^{k+1}\right],\\
&= \sum_{i=1}^{\infty}\frac{\partial Z_i}{\partial y}(x,y)\sum_{k=0}^{\infty}\left[\frac{a_k^i T^k}{k+1}\sum_{j=0}^{k}\left[\binom{k+1}{j}\left(\frac{y}{2}\right)^j\right]\right],
\end{aligned}
\tag{21}
$$

where we used the expansion

$$
(1+a)^b - a^b = \sum_{j=0}^{b-1}\binom{b}{j}a^j.
\tag{22}
$$

Expanding the series to the second order in $y$ and $T$, we get

$$
S_y(x,y) = \sum_{i=1}^{\infty}\frac{\partial Z_i}{\partial y}(x,y)\left[a_0^i+\frac{T}{2}a_1^i+\frac{T^2}{3}a_2^i+y\left(\frac{T}{2}a_1^i+\frac{T^2}{2}a_2^i\right)+\frac{T^2}{4}a_2^i y^2\right],
\tag{23}
$$

where we see that the coefficients of the polynomial in square brackets, responsible for the aliasing into the higher-order modes, are non-zero for all terms. Hence, every time-evolving mode $i$ will contribute to the aliasing into all the radial orders higher than the one of mode $i$.

### 8.3 *Tilt Evolving at Constant Speed*

The case of wavefront consisting only of tilt, $Z_3(x,y)=2y$, evolving at constant speed considered in Sec. 3 is equivalent to $a_k^i=0\ \forall\ i,k$ excluding $i=3$ and $k=1$. The $y$ signal is given as follows:

$$S_y(x,y) = \frac{\partial Z_3}{\partial y}(x,y)\frac{a_1^3 T}{2}\left[\left(1+\frac{y}{2}\right)^2 - \left(\frac{y}{2}\right)^2\right] = a_1^3 T(1+y), \tag{24}$$

and $S_x(x,y) = 0$ because $\partial Z_3/\partial x = 0$. It is straightforward to recognize in the signals above the gradient of a wavefront that is the sum of a tilt mode $Z_3$ of amplitude $a_1^3 T/2$ and of a cylinder mode, defined in Eq. (4), of amplitude $a_1^3 T/8$; this result is in agreement with both the simplified argument in Sec. 3 and numerical simulations shown in Fig. 8.

### 8.4 *Rolling Shutter Case: Edge-to-Center Read-Out Sequence*

If we substitute Eq. (17) for the read-out sequence #2 in Eq. (19), we get

$$S_y(x,y) = \sum_{i=1}^{\infty}\frac{\partial Z_i}{\partial y}(x,y)\sum_{k=0}^{\infty}\frac{a_k^i T^k}{k+1}[(2-|y|)^{k+1} - (1-|y|)^{k+1}]. \tag{25}$$

Expanding the series to the second order in $|y|$ and $T$, we get

$$S_y(x,y) = \sum_{i=1}^{\infty}\frac{\partial Z_i}{\partial y}(x,y)\left[a_0^i + \frac{3T}{2}a_1^i + \frac{7T^2}{3}a_2^i - |y|(a_1^i T + 3T^2 a_2^i) + T^2 a_2^i y^2\right], \tag{26}$$

where we see that the polynomial in square brackets describing the aliasing effect is even in $y$. Therefore, the DIAs are of the same parity as the $i$'th mode that causes them, as clearly visible in the red line of Fig. 11.

## Acknowledgments

The authors wish to thank the adaptive optics teams at Subaru, LAM, and ESO for sharing their experience on the rolling shutter detectors. This work has been partially funded by ADONI—the ADaptive Optics National laboratory of Italy.

## References

1. B. Bigelow et al., "The GMT site, enclosure, and facilities: 2020 design and construction update," *Proc. SPIE* **11445**, 1144508 (2020).
2. B. L. Ellerbroek et al., "TMT adaptive optics program status report," *Proc. SPIE* **8447**, 84471J (2012).
3. R. Tamai and B. Koehler et al., "The ESO's ELT construction progress," *Proc. SPIE* **11445**, 114451E (2020).
4. P. Ciliegi et al., "MAORY: the adaptive optics module for the Extremely Large Telescope (ELT)," *Proc. SPIE* **11448**, 114480Y (2020).
5. B. Neichel et al., "The adaptive optics modes for HARMONI: from Classical to Laser Assisted Tomographic AO," *Proc. SPIE* **9909**, 990909 (2016).
6. J. Crane et al., "NFIRAOS adaptive optics for the Thirty Meter Telescope," *Proc. SPIE* **10703**, 107033V (2018).
7. T. Morris et al., "Adaptive optics for MOSAIC: design and performance of the wide(st)-field AO system for the E-ELT," *Proc. SPIE* **9909**, 99091I (2016).
8. M. Wang et al., "Optical designs of the LGS WFS system for GMT-LTAO," *Proc. SPIE* **8447**, 84473Q (2012).
9. R. Conan et al., "The Giant Magellan telescope laser tomography adaptive optics system," in *Proc. Third AO4ELT Conf.*, S. Esposito and L. Fini, Eds., p. 4 (2013).
10. A. H. Bouchez et al., "An overview and status of GMT active and adaptive optics," *Proc. SPIE* **10703**, 107030W (2018).
11. S. Hippler, "Adaptive optics for extremely large telescopes," *J. Astron. Instrum.* **8**, 1950001 (2019).

12. E. Gendron, "Optical solutions for accommodating ELT LGS wave-front sensing to small format detectors," *Proc. SPIE* **9909**, 99095Z (2016).
13. S. Oberti et al., "LGS tomography and spot truncation: tips and tricks," in *6th Int. Conf. Adapt. Opt. for Extrem. Large Telesc.*, Québec (2019).
14. L. Bardou et al., "ELT-scale elongated LGS wavefront sensing: on-sky results," *Asron. Asrophys.* **649**, A158 (2021).
15. N. Hubin et al., "Adaptive optics for extremely large telescopes," in *Proc. Int. Astron. Union*, Vol. 1 (2006).
16. M. Tallon et al., "Shack–Hartmann wavefront reconstruction with elongated sodium laser guide stars: improvements with priors and noise correlations," *Proc. SPIE* **7015**, 70151N (2008).
17. R. Ragazzoni et al., "Extending the pyramid WFS to LGSs: the INGOT WFS," *Proc. SPIE* **10703**, 1106–1111 (2018).
18. J. W. Beletic, "Follow the yellow-orange rabbit: a CCD optimized for wavefront sensing a pulsed sodium laser guide star," *Proc. SPIE* **5499**, 302–309 (2004).
19. M. Downing et al., "LGSD/NGSD: high speed optical CMOS imagers for E-ELT adaptive optics," *Proc. SPIE* **9154**, 91540Q (2014).
20. J. Reyes-Moreno, M. Downing, and N. D. Lieto, "ESO adaptive optics NGSD/LGSD detector and camera controller for the E-ELT," *Proc. SPIE* **9909**, 1759–1772 (2016).
21. P. Feautrier et al., "Advances in detector technologies for visible and infrared wavefront sensing," *Proc. SPIE* **8447**, 84470Q (2012).
22. M. Downing et al., "Update on development of WFS cameras at ESO for the ELT," *Proc. SPIE* **10703**, 107031W (2018).
23. F. Rigaut et al., "A conceptual design study for Subaru ULTIMATE GLAO," *Proc. SPIE* **10703**, 1070324 (2018).
24. M. Dirnberger et al., "Rolling shutter detector data flow strategies to push the limits of AO performance," *Proc. SPIE* **10703**, 107034O (2018).
25. M. S. Belen'kii, "Tilt angular anisoplanatism and a full-aperture tilt-measurement technique with a laser guide star," *Appl. Opt.* **39**(33), 6097–6108 (2000).
26. C. Plantet et al., "Spatio-temporal statistics of the turbulent piston-removed phase and Zernike coefficients for two distinct beams," *J. Opt. Soc. Am. A* **39**, 17–27 (2021).
27. J.-M. Conan, G. Rousset, and P.-Y. Madec, "Wave-front temporal spectra in high-resolution imaging through turbulence," *J. Opt. Soc. Am. A* **12**(7), 1559–1570 (1995).
28. M. Sarazin et al., "Defining reference turbulence profiles for E-ELT AO performance simulations," in *Proc. Third AO4ELT Conf.*, S. Esposito and L. Fini, Eds., p. 89 (2013).
29. B. Neichel et al., "Gemini multiconjugate adaptive optics system review – II. Commissioning, operation and overall performance," *MNRAS* **440**, 1002–1019 (2014).
30. S. Oberti et al., "The AO in AOF," *Proc. SPIE* **10703**, 107031G (2018).
31. R. J. Noll, "Zernike polynomials and atmospheric turbulence," *J. Opt. Soc. Am.* **66**, 207–211 (1976).
32. G. Agapito, A. Puglisi, and S. Esposito, "PASSATA: object oriented numerical simulation software for adaptive optics," *Proc. SPIE* **9909**, 99097E (2016).
33. N. Thatte et al., "HARMONI: the ELT's first-light near-infrared and visible integral field spectrograph," *The Messenger* **182**, 7–12 (2021).
34. P. Ciliegi et al., "MAORY: a multi-conjugate adaptive optics RelaY for ELT," *The Messenger* **182**, 13–16 (2021).
35. T. Fusco et al., "A story of errors and bias: the optimization of the LGS WFS for HARMONI," in *AO4ELT6*, Québec (2019).
36. R. Ragazzoni, "Pupil plane wavefront sensing with an oscillating prism," *J. Mod. Opt.* **43**, 289–293 (1996).
37. F. Rigaut and E. Gendron, "Laser guide star in adaptive optics: the tilt determination problem," *Astron. Astrophys.* **261**, 677–684 (1992).
38. P. L. Wizinowich et al., "The W. M. Keck Observatory laser guide star adaptive optics system: overview," *Publ. Astron. Soc. Pac.* **118**, 297–309 (2006).
39. R. M. Clare, M. A. van Dam, and A. H. Bouchez, "Modeling low order aberrations in laser guide star adaptive optics systems," *Opt. Express* **15**, 4711–4725 (2007).

40. M. A. van Dam et al., "Design of a truth sensor for the GMT laser tomography adaptive optics system," *Proc. SPIE* **8447**, 844717 (2012).
41. A. Riccardi et al., "The ERIS adaptive optics system," *Proc. SPIE* **9909**, 99091B (2016).
42. E. Mieda et al., "Testing the pyramid truth wavefront sensor for NFIRAOS in the lab," *Proc. SPIE* **9909**, 99091J (2016).
43. L. Busoni et al., "Adaptive optics design status of MAORY, the MCAO system of European ELT," in *6th Int. Conf. Adap. Opt. Extrem. Large Telesc.*, Québec (2019).
44. Y. G. Lee and G. Kai, "Fast-rolling shutter compensation based on piecewise quadratic approximation of a camera trajectory," *Opt. Eng.* **53**(9), 093101 (2014).
45. C.-K. Liang, L.-W. Chang, and H. H. Chen, "Analysis and compensation of rolling shutter effect," *IEEE Trans. Image Process.* **17**(8), 1323–1330 (2008).
46. C. Dessenne, P.-Y. Madec, and G. Rousset, "Optimization of a predictive controller for closed-loop adaptive optics," *Appl. Opt.* **37**, 4623–4633 (1998).
47. L. A. Poyneer and J.-P. Véran, "Toward feasible and effective predictive wavefront control for adaptive optics," *Proc. SPIE* **7015**, 70151E (2008).
48. D. Del Moro et al., "Improvements on adaptive optics control approaches: experimental tests of wavefront correction forecasting," *J. Astron. Telesc. Instrum. Syst.* **1**, 019002 (2015).
49. M. A. van Kooten et al., "Status of predictive wavefront control on Keck II adaptive optics bench: on-sky coronagraphic results," *Proc. SPIE* **11823**, 118231F (2021).
50. C. Petit et al., "SPHERE eXtreme AO control scheme: final performance assessment and on sky validation of the first auto-tuned LQG based operational system," *Proc. SPIE* **9148**, 91480O (2014).
51. O. Lardière et al., "Performance comparison of centroiding algorithms for laser guide star wavefront sensing with extremely large telescopes," *Appl. Opt.* **49**, G78 (2010).

**Guido Agapito** is a researcher at INAF, Osservatorio Astrofisico di Arcetri, Adaptive Optics Group. He has more than 10 years of experience in AO for astronomy, and he is currently involved in several projects, including Multiconjugate Adaptive Optics RelaY (MAORY) for ELT, Enhanced Resolution Imager and Spectrograph (ERIS), MCAO-Assisted Visible Imager and Spectrograph (MAVIS), and Single conjugated adaptive Optics Upgrade for LBT (SOUL). He is an expert of AO control systems, and he is the main developer of the PyrAmid Simulator Software for Adaptive OpTics Arcetri (PASSATA).

**Lorenzo Busoni** is a researcher at INAF, Osservatorio Astrofisico di Arcetri, Adaptive Optics Group since 2005. He is currently AO engineer of the MAORY for ELT.

Biographies of the other authors are not available.